JGR Oceans

RESEARCH ARTICLE
10.1029/2020JC016366

Importance of Boundary Processes for Heat Uptake in the Subpolar North Atlantic

D. G. Desbruyères[1], B. Sinha[2], E. L. McDonagh[3,2], S. A. Josey[2], N. P. Holliday[2], D. A. Smeed[2], A. L. New[2], A. Megann[2], and B. I. Moat[2]

[1]Ifremer, University of Brest, CNRS, IRD, Laboratoire d'Océanographie Physique et Spatiale, Plouzané, France, [2]National Oceanography Centre, Southampton, UK, [3]NORCE, Norwegian Research Centre, Bjerknes Centre for Climate Research, Bergen, Norway

Key Points:
- A causal and lagged relationship exists between basin-mean upper and intermediate decadal temperature changes in the subpolar North Atlantic
- Variability in vertical heat transport convergence is dominant within the energetic boundary currents of the subpolar North Atlantic
- Open-ocean deep convection is not a unique pathway for slow thermohaline ventilation and heat uptake in the subpolar North Atlantic

Supporting Information:
- Data Set S1
- Data Set S2
- Data Set S3

Correspondence to:
D. G. Desbruyères,
damien.desbruyeres@ifremer.fr

Citation:
Desbruyères, D. G., Sinha, B., McDonagh, E. L., Josey, S. A., Holliday, N. P., Smeed, D. A., et al. (2020). Importance of boundary processes for heat uptake in the subpolar North Atlantic. *Journal of Geophysical Research: Oceans*, *125*, e2020JC016366. https://doi.org/10.1029/2020JC016366

Received 22 MAY 2020
Accepted 5 JUL 2020
Accepted article online 7 JUL 2020

Abstract The decadal to multidecadal temperature variability of the intermediate (700–2,000 m) North Atlantic Subpolar Gyre (SPG) significantly imprints the global pattern of ocean heat uptake. Here, the origins and dominant pathways of this variability are investigated with an ocean analysis product (EN4), an ocean state estimate (ECCOv4), and idealized modeling approaches. Sustained increases and decreases of intermediate temperature in the SPG correlate with long-lasting warm and cold states of the upper ocean with the largest anomalous vertical heat exchanges confined to the vicinity of continental boundaries and strong ocean currents. In particular, vertical diffusive processes along the boundaries of the Labrador, Irminger, and Newfoundland basins are important drivers of the recent intermediate depth warming trend observed during 1996–2014. The overall effect of those processes is captured by a one-dimensional diffusive model with appropriate boundary-like parametrization and demonstrated through the boundary-focused downward propagation of a passive tracer in a 3-D numerical simulation. Our results imply that the slow and quasi-periodic ventilation of intermediate thermohaline properties and associated heat uptake in the SPG are not strictly driven by convection-restratification events in the open seas but also receives a key contribution from boundary sinking and mixing. Increased skill for modeling and predicting intermediate-depth ocean properties in the North Atlantic will hence require the appropriate representation of surface-deep dynamical connections within the boundary currents encircling Greenland and Newfoundland.

Plain Language Summary The subarctic basins of the North Atlantic Ocean play a fundamental role in regulating the climate system. This occurs notably throughout direct connections between the ocean surface (and hence the atmosphere) and deep oceanic layers, which enable the long-term sequestration and subsequent propagation of physical and biogeochemical anomalies (e.g., heat and carbon). Here, we employ a multitool approach to investigate the mechanisms by which anomalous heat can penetrate downward in this region. Historical observations gathered during 1950–2016 and combined with idealized modeling strategy suggest that decadal temperature trends in the intermediate layer strongly correlate with long-lasting warm and cold states of the upper ocean, suggesting potential for first-order predictability. Focusing on the well-observed era (1992–2016) using a realistic ocean reanalysis and tracer propagation experiments in a numerical model, we show that the associated downward penetration of temperature anomalies receives an important contribution from mixing and advection within the energetic boundary currents of the Labrador Sea, Irminger Sea, and Newfoundland basin.

1. Introduction

The global ocean is currently warming at a rate of 0.6–0.8 W m^{-2} due to a persistent and human-induced imbalance of the radiative forcing at the top of the atmosphere (Johnson et al., 2016; Liu et al., 2015). Sustained ocean observing systems (Riser et al., 2016; Talley et al., 2016) indicate that half of this warming is confined to the upper 700 m of the water column (18% of the global ocean volume), the remainder being stored in deeper oceanic layers (Desbruyères et al., 2017). The extent to which the deep interior will continue to absorb anthropogenic heat is an essential question for environmental projections and requires an understanding of the many mechanisms influencing the deep thermal structure of ocean basins. Among those basins, the Subpolar Gyre (SPG) of the North Atlantic Ocean plays a major role in connecting surface and deep oceanic layers and undergoes decadal-scale variability that can significantly imprint global averages

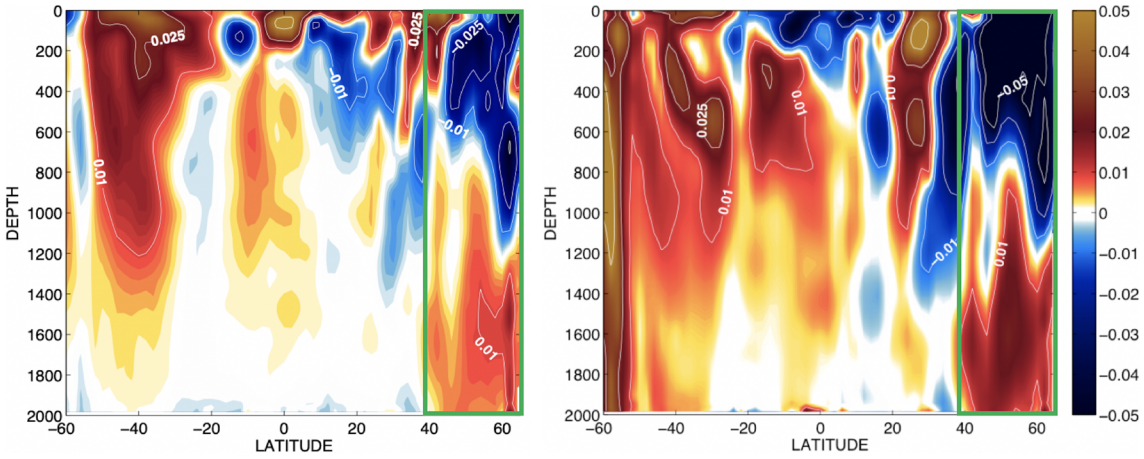

Figure 1. Zonal average of linear temperature change (°C year^{-1}) during 2006–2016 as measured between the surface and 2,000 m depth by the Argo array of autonomous profiling floats within the (left) global and (right) Atlantic Ocean. The green rectangle highlights the peculiar vertical structure of the trend in the North Atlantic SPG that motivates the present analysis.

(Chen & Tung, 2014; Drijfhout et al., 2014; Robson et al., 2018). A striking signal was particularly captured by the Argo network of profiling floats during the latest decade or so (2006–2016) when the SPG rapidly cooled in the upper layer while warming below, with a noticeable impact on the vertical pattern of global ocean heat uptake (Robson et al., 2018) (Figure 1).

The mechanisms driving multidecadal basin-averaged trends in the ocean heat content (OHC) of the upper layer (0–700) of the SPG are now relatively well studied and have been described from both observational and modeling approaches. They are known to mimic sea surface temperature changes averaged over the whole North Atlantic—the Atlantic multidecadal variability (AMV) index—and to be primarily driven by changes in the large-scale ocean circulation (Chafik et al., 2019; Desbruyères et al., 2019; Frajka-Williams et al., 2017; McCarthy et al., 2015; Moat et al., 2019; Piecuch et al., 2017) with a more intermittent role of air-sea heat exchanges (Josey et al., 2018). The drivers of deeper OHC trends and their relationship with upper layer variability remain, on the other hand, more obscure. Intermittent and open-ocean deep convection within the marginal seas surrounding Greenland, triggered by intense surface buoyancy loss of a pre-conditioned water column, has been often depicted as a dominant process for propagating surface signals downward and renewing intermediate and deep-water mass properties (Yashayaev & Loder, 2016). In the interior of the Labrador and Irminger Seas, deep convection events are regionally most intense—sometimes reaching down below 2,000 m—but weather-dependent and therefore temporally intermittent. The dominant interannual character of intermediate water mass renewal rates in the SPG suggested by historical observations—and best depicted by potential vorticity variability—is in fact seemingly in contrast with the multidecadal time scale of deep temperature and salinity signals (Van Aken et al., 2011). For instance, the convective event of the early 1990s—the most intense on record—formed a voluminous Labrador Sea water (LSW) vintage and drove a rapid cooling of the intermediate layer, which yet occurred *within* a gradual cooling trend observed since the early 1970s. This suggests that cold (and fresh) anomalies may have propagated down the water column via additional routes and processes distinct from locally forced and deep convective chimneys in the gyre interior.

Modeling studies also support the idea that regions where open-ocean deep convection occurs do not necessarily correspond to the regions where the low-frequency ventilation of the deep ocean is strongest, and an important contribution of confined western boundary processes to this deep ventilation has been suggested (MacGilchrist, 2017; Spall & Pickart, 2001). In fact, the boundary region of the SPG, encompassing strong boundary currents above the continental slopes (Daniault et al., 2016; Handmann et al., 2018), is known to host important Eulerian and eddy-driven vertical fluxes and sinking processes capable of connecting upper and deep oceanic layers (Katsman et al., 2018; Le Bras et al., 2020; Spall, 2010; Straneo, 2006). Observations have further revealed recurrent shallow convection and formation of LSW directly in the boundary current (Palter et al., 2008), mid-depth mesoscale activity, and intense diapycnal diffusion around the tips of Greenland and Newfoundland (Lauderdale et al., 2008; Stöber et al., 2008), as well as across-slope

cascading of dense shelf water in the Irminger Sea (Falina et al., 2012). The combined role of such boundary processes in injecting decadal temperature anomalies into the deep interior remains largely unknown and unquantified.

Using ocean observations, an ocean state estimate and simple modeling approaches (1-D modeling and tracer experiment), this paper seeks to inform on the decadal to multidecadal temperature variability observed in the intermediate layer (700–2,000 m) of the North Atlantic SPG and its relationship with upper ocean state. We particularly aim to investigate the importance of boundary-intensified vertical heat exchange for the heat budget of the region. After presenting the historical observational context (1950–2016), the study focuses on the drivers and pathways of the most recent warming trend that took place in the intermediate layer during 1996–2014.

2. Methods

2.1. Observational Datasets and Derived Variables

The hydrographic dataset used herein is the 1950–2016 EN4.2.0 product of gridded potential temperature (θ) and practical salinity (S) profiles (Good et al., 2013). The product is on a 1° longitude/latitude grid and has 42 vertical levels with spacing ranging from 10 m near the surface to 300 m in the abyss. In this study we retained the 1° grid, and at each grid point, θ and S profiles were interpolated to a regular 20 db vertical spacing. Practical salinity was converted to absolute salinity and potential temperature to conservative temperature using the TEOS-10 Gibbs Sea Water (GSW) toolbox. GSW was also used to compute σ_0 (potential density relative to sea surface). Monthly fields of absolute salinity, conservative temperature, and derived quantities were averaged into annual mean fields. For each of the above-mentioned variables, anomalies were obtained by removing the long-term 1950–2016 mean and the long-term 1950–2016 linear trend at each grid point.

2.2. One-Dimensional Diffusion Model

A one-dimensional model of vertical diffusion (see Equation 2) was solved numerically using a standard backward time-centered space (BTCS) discretization with thirty 100 m-thick layers, time integrated for 67 years with a time step of 1 day. Several numerical iterations were performed to ensure the convergence of the solution. Details about the relevant parameterization and initial/boundary conditions are provided in the main text (section 3).

2.3. Tracer Experiments

A 3-D advection–diffusion model is solved on a subset of the NEMO ORCA025 ocean model grid (Madec et al., 2019) spanning 71.5–35°W, 44.5–67°N, covering the Labrador Sea and part of the North Atlantic. The model uses a leapfrog time step with formal error O (Δt^2), an upstream (i.e., non-diffusive) differencing scheme for the 3-D advective terms with formal O (Δx), and an implicit treatment of the vertical diffusion with error O (Δz^2). We neglect horizontal diffusion. To achieve computational stability for this simple numerical system, we employ a vertical resolution of 2.25 m, a time step of 400 s (an occasional forward time step is included to avoid development of a computational mode), and a vertical diffusivity of 3×10^{-3} m^2 s^{-1} (to correspond with the 1-D vertical diffusion model of Equation 1). Those choices logically depend on the model resolution, and a higher (resp. lower) effective diffusivity coefficient would notably be required if a higher (resp. lower) resolution model was being used. We set $\frac{\partial \theta_d}{\partial z} = 0$ at the ocean surface and at the sea floor (θ_d is the temperature tracer anomaly), so there is no surface flux input of tracer and no diffusive loss through the bottom. Tracer is not allowed to advect horizontally or vertically into the coast or into the sea floor/bottom topography, but can be advected horizontally out of the computational domain. The advection velocities are obtained from the annual-mean three-dimensional velocity field from year 1978 of a forced simulation of the NEMO model on the ORCA025 grid (Megann et al., 2014). The model is integrated for 25 years to correspond to the ECCOv4 time period (1992–2016; see section 2.4). Initially, the tracer concentration is set to zero everywhere. An inflow is set up at the northeastern boundary (43.5°W, 59.5–60°N, 0–230 m depth) by relaxing the tracer values there to −0.8 K during years 1–10 of the integration, to +0.8 K during years 11–20 and back to −0.8 K during years 20–25 (to correspond with the sequence of anomalies seen in ECCOv4 and EN4 during 1992–2016).

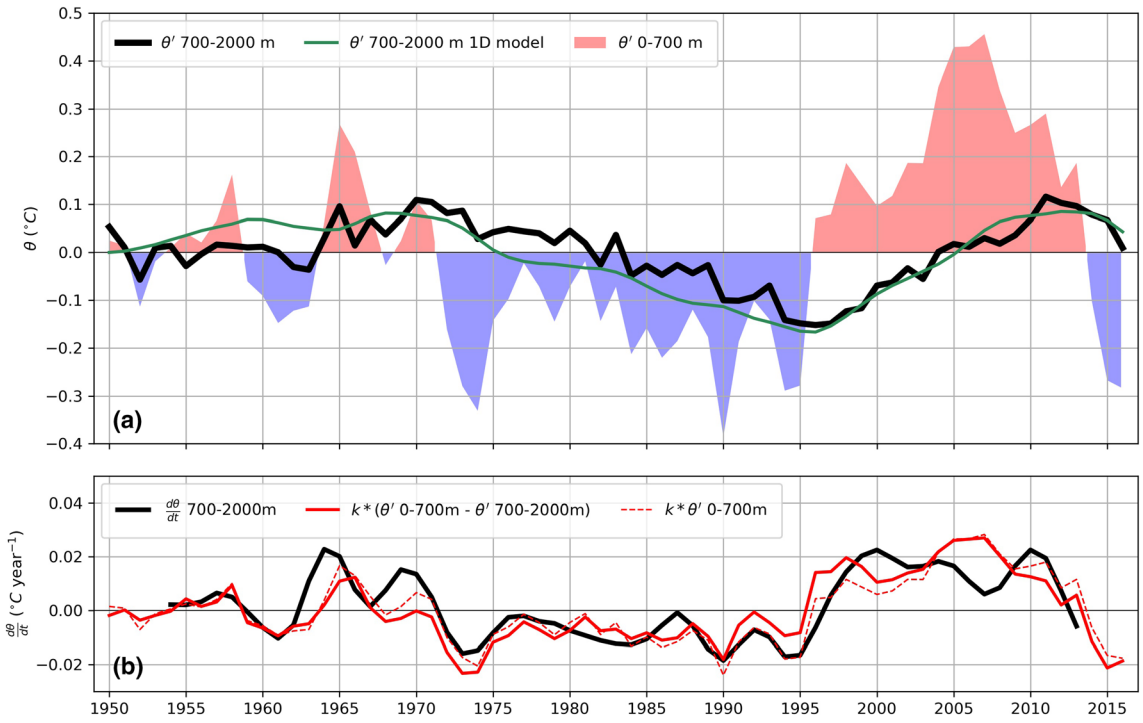

Figure 2. (a) Observed temperature anomalies within the 0–700 m (shadings) and the 700–2,000 m (thick black) layers in the SPG (63–10°W and 45–67°N). Data taken from the gridded EN4.2.1 product (Good et al., 2013). The green line shows temperature anomalies within 700–2,000 m as simulated by a 1-D diffusive model forced by the observed surface temperature time series (Equation 2). (b) The observed components of the two-layer ocean model (Equation 1 with heat exchange coefficient $k = 0.06$ year^{-1}). The dashed line shows the contribution of 0–700 m anomalies.

2.4. Ocean Reanalysis ECCOv4

The state-of-the-art ocean state estimates ECCO (Estimating the Circulation and Climate of the Ocean) are based on least-squares fitting of the Massachusetts Institute of Technology General Circulation Model to numerous types of global-scale ocean observations during 1992–2016. Known equation of motions and conservation laws are satisfied within ECCO, making this state estimate an appropriate tool for heat budget analysis. It is thoroughly described elsewhere, and we here only provide a brief description (Forget et al., 2015). The state estimate is built from a global general circulation model (Marshall et al., 1997) on a spatial grid with 1° nominal horizontal resolution and 50 vertical layers. The effect of non-resolved dynamics is parametrized using common schemes (Gaspar et al., 1990; Gent & Mcwilliams, 1990; Redi, 1982). The model solution is iteratively adjusted to satisfy observational constraint and precomputed uncertainty estimates. Surface buoyancy forcing (heat and freshwater) is derived from bulk formulae with initial conditions taken from the European Centre for Medium-Range Weather Forecasts Reanalysis-Interim (ERA-Interim). We here use the ECCOv4 Release 3 (Forget et al., 2015).

3. The Multidecadal Observational Context

The SPG is defined throughout the paper as the region bounded by 63–10°W and 45–67°N, with the exclusion of shelf seas (bathymetry < 500 m). Historical observations gathered in this region from the early 1950s to present day show that the multidecadal fluctuations of temperature above 700 m resemble the AMV index derived from sea surface temperature (Frajka-Williams et al., 2017), with a succession of three main phases separated by relatively abrupt shifts: a warm state during 1955–1971, a cold state during 1972–1995, and a warm state during 1996–2014 (Figure 2a, red and blue shadings). As noted earlier, this cycle is known to be dominantly driven by anomalous horizontal heat transport convergence, including spin-ups and spin-downs of the horizontal and vertical circulations and horizontal redistribution of water masses, with comparatively minor role of local atmospheric forcing.

Temperature within the intermediate layer (700–2,000 m) of the SPG exhibits a succession of multidecadal trends, with a periodic time scale of about 50 years and magnitudes reaching ±0.015°C year^{-1} (Figure 2a,

Table 1
The Statistics of the Pearson Correlations and Associated 95% Confidence Intervals Between 700 and 2,000 m Heat Content Tendency and Its Total/Horizontal/Vertical Advective and Diffusive Components, As Well As With the 0–700 Heat Content Change

X		*Y*	*R*	95% CI
EN4	$TEND_{700–2,000m}$	$OHC_{0–700m} - OHC_{700–2,000m}$	0.75	[0.62–0.85]
ECCOV4	$TEND_{700–2,000m}$	$OHC_{0–700m} - OHC_{700–2,000m}$	0.85	[0.68–0.93]
		$ADV_{700–2,000m}$	0.81	[0.6–0.91]
		$HADV_{700–2,000m}$	0.05	[−0.36–0.44]
		$VADV_{700–2,000m}$	0.74	[0.47–0.88]
		$DIF_{700–2,000m}$	0.85	[0.67–0.93]
		$HDIV_{700–2,000m}$	−0.44	[−0.72 to −0.04]
		$VDIF_{700–2,000m}$	0.86	[0.69–0.94]

Note. Correlations between any variables *X* and *Y* were performed on annually averaged and detrended time series. The confidence intervals were obtained following common practice, that is by calculating *p*-values from the *t*-statistic $T = r\frac{\sqrt{N-2}}{\sqrt{1-r^2}}$ (one-tailed test) where *N* the number of degrees of freedom taken here as the number of years minus two. Correlations and confidence intervals were obtained using the numerical tools of Vallat (2018).

black line). Those trends include a warming during 1955–1971, a long-term cooling during 1972–1995, and a warming until 2014. A simple depth-space definition of the intermediate layer is here chosen for consistency with common practice in the quantification and depiction of global and regional heat content trends (Cheng et al., 2017; Desbruyères et al., 2017; Rhein et al., 2013). Therefore, our approach aims towards large-scale fixed-volume heat budget calculations (section 4), rather than local density-space water mass analyses.

As demonstrated in a previous analysis of historical observations, multidecadal temperature variability in the intermediate layer is largely *density-compensated*, reflecting correlated temperature and salinity anomalies spreading as passive tracers within the lower limb of the large-scale overturning circulation (Mauritzen et al., 2012). Importantly, the signature of strong and intermittent deep convection events (e.g., late 1950s and early 1990s) is not readily discernible within this low-frequency variability (Van Aken et al., 2011). Rather, this multidecadal signal appears here related to persistent anomalous forcing from the upper ocean: when the 0–700 m layer is anomalously warm or cold, the layer below warms up or cools down, respectively. This response can be first evidenced through a simple two-layer ocean model (Gregory, 2000):

$$\frac{d\theta_{700–2,000m}}{dt} = k\left(\theta_{0–700m} - \theta_{700–2,000m}\right) \quad (1)$$

with k being a heat exchange coefficient between the upper layer and the intermediate layer and θ_{0-700m} and $\theta_{700-2,000m}$ their respective temperature variations. The temperature tendency in the intermediate layer computed from the temperature difference between successive 1st of Januarys (left-hand side term) is remarkably proportional to the temperature difference between the two layers (right-hand side term, r = 0.75, significant at the 95% level, Table 1), a term interpreted here as a linear representation of vertical heat transport by all processes (Figure 2b). The bulk of this vertical temperature differences is, as expected, largely driven the upper layer AMV-like signal.

The connection between the upper and intermediate layers is also identified by the progressive downward propagation of the upper warm-cold-warm cycle down to about 2,000 m depth (Figure 3a). The extreme convection event of the mid-1990s, associated with a cooling signal peaking approximately 1,700 m depth, appears as an important interannual event embedded within but not exclusively driving this low-frequency pattern. The physical mechanisms controlling such an apparent downward propagation of low-frequency surface signals are likely multiple, including Eulerian and eddy-driven vertical advection, open-ocean and boundary current convection, diffusion, or across-slope cascading. Although those processes cannot be explicitly resolved using "low-resolution" observational datasets, we show here that their net effect can be effectively reproduced by a 1-D diffusion model (see section 2):

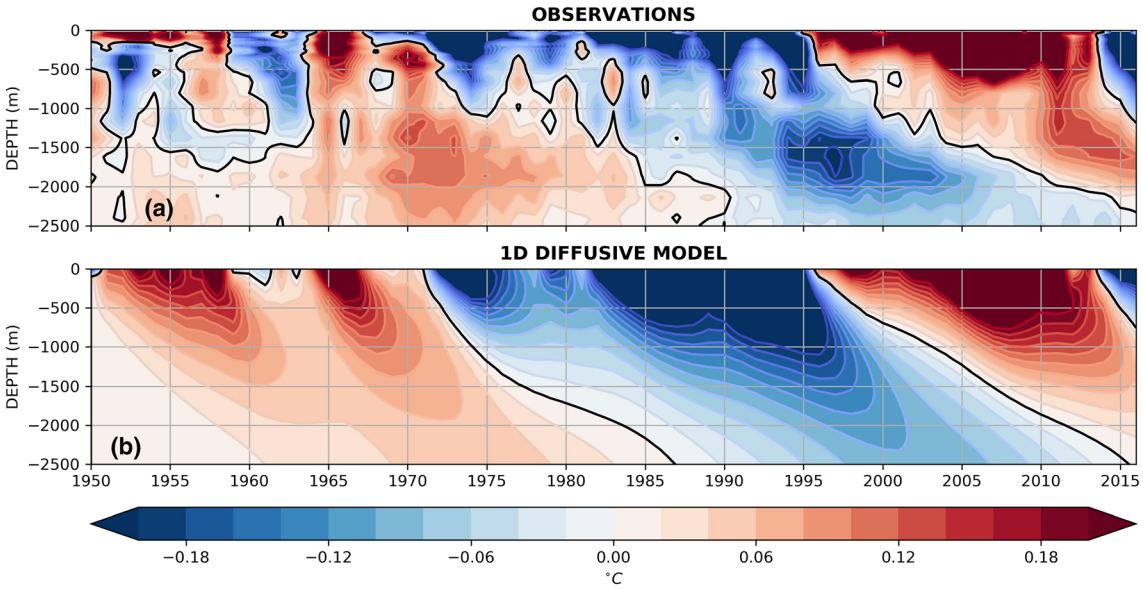

Figure 3. (a) The depth-time diagram of observed temperature anomalies averaged in the SPG (gridded EN4.2.1 product). White line is the aggregate maximum mixed layer depth in the western SPG (55–65°N to 40–60°W) computed as the 75th percentile of the pycnostad depths (Yashayaev & Loder, 2016). (b) The solution of a simple 1-D diffusive model initialized with surface anomalies in the SPG (see text for details).

$$\frac{\partial \theta_d(z,\,t)}{\partial t} = \kappa \frac{\partial^2 \theta_d(z,\,t)}{\partial z^2} \tag{2}$$

where $\theta_d(z,\,t)$ is the temperature anomaly and κ is a chosen constant coefficient for vertical diffusivity. Boundary conditions are set as $\theta_d(-H,\,t) = 0$ at the bottom ($H = 4{,}000$ m) while the observed surface temperature averaged in the SPG is prescribed as surface conditions. Initial conditions are set as $\theta_d(z,\,0) = 0$. The vertical diffusivity coefficient is set as $\kappa = 3 \times 10^{-3}$ m^{-2} s^{-1}—a value situated within the upper range of observed vertical diffusivities within the SPG yet not uncommon along steep continental slopes (Stöber et al., 2008; Walter et al., 2005; Whalen et al., 2012). Here, κ does not represent solely diffusion, but is an effective diffusivity coefficient which we interpret as the net effect of the various types of vertical heat transports mentioned above and their occurrence within the energetic boundary region of the SPG, as will be discussed later. The low-frequency downward propagation of temperature anomalies is well reproduced by the simple model (Figure 3b), and the overall amplitude and phase of the intermediate temperature signal appear quite similar to that observed (Figure 2a red line). This further suggests that the renewal of properties in the intermediate layer of the SPG is importantly impacted by the *time-independent* sinking of multidecadal surface anomalies.

While the historical observational record can be satisfactorily used for basin-integrated metrics, it may be inadequate for investigating the basin-scale horizontal patterns of temperature changes, most particularly at intermediate and deep levels where observations are limited to spatially and temporally localized shipboard hydrographic sections. The sustained and homogeneous network of Argo profiling float has become appropriate for capturing the horizontal pattern of temperature changes within both the upper and intermediate layers from about 2005 (Riser et al., 2016; Roemmich et al., 2015). The 2005–2014 temperature trend averaged between 700 and 2,000 m shows warming over most of the western SPG and a relatively weaker cooling trend in the east (Figure 4a). Strongest positive values are found along the interior path of the North Atlantic current (NAC), spreading north and east from the area surrounding Newfoundland. This pattern—strictly representative of the considered time span—can reflect either a change in the local circulation, a local injection of upper temperature trends, and/or the late arrival of temperature trends that were sunk upstream and subsequently advected by the southward-flowing Deep Western Boundary Current (DWBC) before being entrained by the NAC within the SPG interior.

Because basin-integrated metrics highlight the potential key role of the large-scale upper ocean temperature anomalies in driving deeper temperature trends (Figure 2), we show in Figure 4b the distribution of

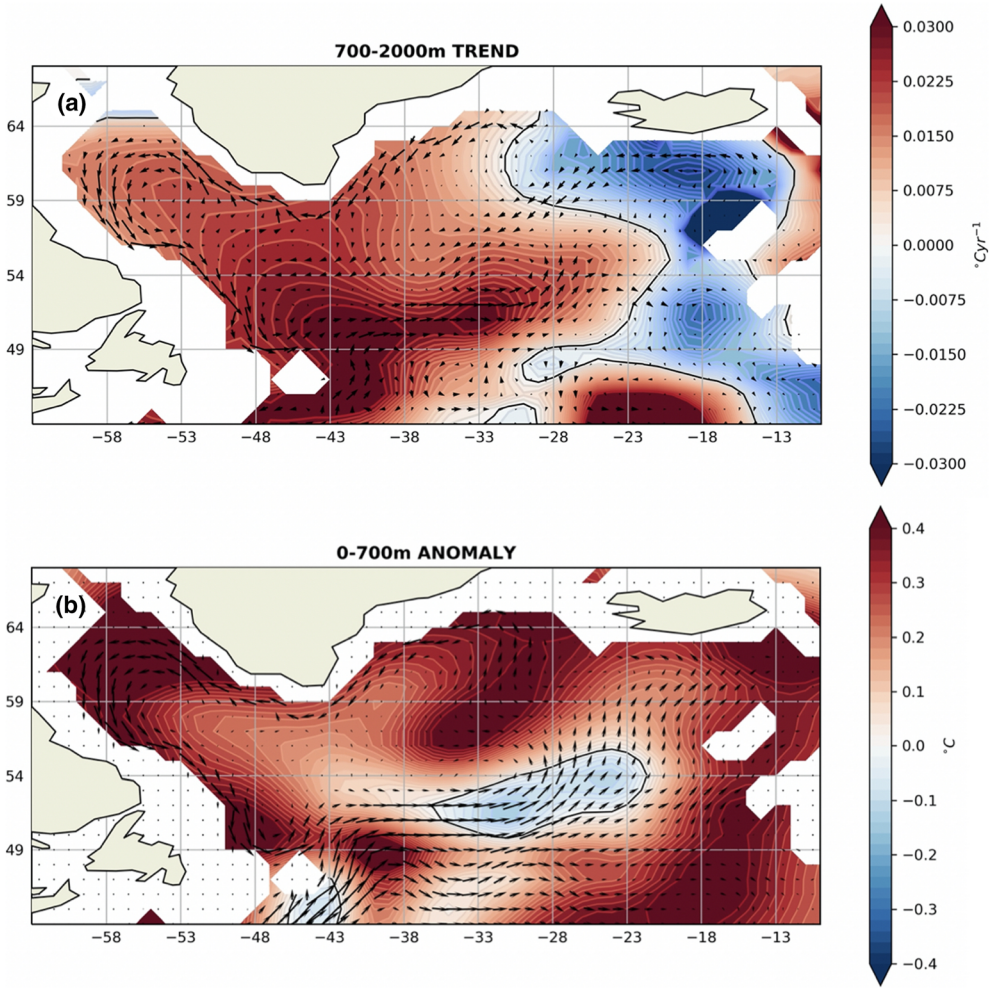

Figure 4. (a) The observed 2005–2014 temperature trend averaged within the intermediate 700–2,000 m layer (in °C year^{-1}). Black arrows show time-mean Argo-derived horizontal currents averaged within 700–2,000 m (from Colin de Verdière et al., 2019). (b) The observed 2005–2014 temperature anomalies relative to the long-term 1950–2016 mean averaged within the upper 0–700 m layer. Black arrows show time-mean Argo-derived horizontal currents averaged within 0–700 m (from Colin de Verdière et al., 2019).

temperature anomalies (relative to the long-term mean) above 700 m during 2005–2014. The strongest positive anomalies are found along the cyclonic path of the boundary current—from Rockall Trough down to Flemish Cap—which is therefore likely to represent an important gateway for surface decadal-scale temperature signals to enter the intermediate layer. In fact, the confined boundary regions of both the Newfoundland area and the Irminger and Labrador seas are known to host the most significant vertical mass exchanges within the SPG domain, as demonstrated by theory and recently illustrated with a very high-resolution simulation (Sayol et al., 2019). Moreover, basin-scale observations of fine scale velocity and density variance show that the boundaries of the Labrador and Flemish Cap areas also host the most intense vertical mixing within the whole SPG region (Walter et al., 2005).

4. Heat Budget of the Intermediate Layer

In order to identify the dominant mechanism of (anomalous) heat content redistribution between the upper and intermediate layer of the SPG, we analyze the outputs of an ocean state estimate (ECCOv4) that assimilates various types of ocean observations in a dynamically coherent manner, thereby enabling the closure of realistic oceanic heat budgets over the period 1992–2016 (Forget et al., 2015). This particular assimilated model was found to be a good fit to observations of global-scale and basin-scale ocean heat content and

circulation (Piecuch et al., 2017), and to represent an efficient tool for studying ocean vertical heat transport and its decadal changes (Liang et al., 2015; Liang, Piecuch, et al., 2017; Liang, Spall, et al., 2017). The conservation rules specific to this model imply that there are no unidentified sources of heat, making it most suitable for investigating realistic regional ocean heat budgets and the underlying mechanisms.

In ECCO the surface forcing term penetrates the water column vertically and decays exponentially over the top 200 m. Following Piecuch et al. (2017), we write the budget equation for the OHC rate of change of the 700–2,000 m intermediate layer as

$$C_p\rho_0\int_t\int_V\frac{\partial\theta}{\partial t}dVdt = C_p\rho_0\int_t\int_V -\nabla(\vec{u}\theta)dVdt + C_p\rho_0\int_t\int_V D_\theta dVdt \quad (3)$$

which we symbolize as

$$T = A + M$$

Here C_p is the specific heat capacity, ρ_0 is a reference density, V is the volume, θ is the potential temperature, $\vec{u}$ is the three-dimensional velocity vector, and D_θ is the parametrized mixing. Note that $\vec{u}$ contains both resolved Eulerian and parametrized (eddy-driven) bolus contributions, while D_θ includes both diapycnal and isopycnal diffusion, as well as contributions from mixed layer turbulence and convective instabilities. For clarity, we will refer to the overall diffusive term as *combined diffusion*. The term on the left-hand side of Equation 4 is the total OHC change (T, units of Joules). The first and second terms on the right-hand side of Equation 4 are the advective heat convergence (A) and the diffusive heat convergence (M), respectively. We will refer in the following to the time derivative of those terms as T_t, A_t, and M_t (units of Watts).

A first measure of the variability (standard deviation) of A_t and M_t is in line with theoretical and high-resolution modeling studies, with values being stronger along the SPG boundary and surface current pathways and weaker in the basin interiors (Figures 5a and 5b). Those clear boundary-intensified patterns have three main and common centers of action: the northern boundary of the Irminger Sea, the western and eastern boundary of the Labrador Sea, and the area surrounding Flemish Cap and Newfoundland. Comparatively, regions of deepest mixed layer, found in ECCOv4 in the central Labrador Sea, are characterized by relatively weak variability in A_t and M_t. Rather, the horizontal pattern of standard deviation in A_t and M_t appear linked to the 1992–2016 mean distribution of eddy kinetic energy (EKE) in the intermediate layer (Figure 5c) derived from ECCOv4 velocities, with highest values within the western boundary currents of the SPG, from Greenland to Newfoundland, and along the NAC path.

Following the observation-based two-layer model (Figure 2b), we verify that the simulated T_t within the intermediate 700–2,000 m layer is well correlated with the difference in T between the upper and intermediate layers and hence with the AMV-like succession of warm and cold upper ocean states ($r = 0.85$, significant at the 95% level, Figure 6a, Table 1). We further decompose the heat budget time series into its three components (tendency T, advection A, and diffusion M) and show their evolution as anchored to the 1992 initial conditions (Figure 6b). As expected, the evolution of T reproduces well the observed pattern, with a cooling until 2005 followed by a long-term warming until 2014, and an emerging cooling afterwards. Both A and M are importantly involved and seem to covary for most of the period except during the most recent years. The basin-average covariance ratio for advective and diffusive heat fluxes, computed as $\frac{\sigma(A_t,\ T_t)}{\sigma(T_t)^2}$ and $\frac{\sigma(M_t,\ T_t)}{\sigma(T_t)^2}$, respectively amount to 46% and 54%, with those values themselves largely explained by the vertical component of the fluxes (85% and 103%, respectively). In particular, two-thirds of the dominant warming trend of the intermediate layer during 1996–2013 is explained by the vertical component of combined diffusive heat fluxes M. The depth-time distribution of the heat budget terms (Figure 7) further highlights the important role of combined diffusion in the model in spreading the decadal upper temperature signals downward, in close agreement with the observed and 1-D-modeled patterns previously described (Figure 3).

The horizontal distribution of the heat budget components averaged during the 1996–2013 warming phase of the intermediate layer is shown in Figure 8. The horizontal pattern of T_t resembles the observation-based pattern of temperature trend seen in Figure 4a, with a basin-wide warming marked by a major center of

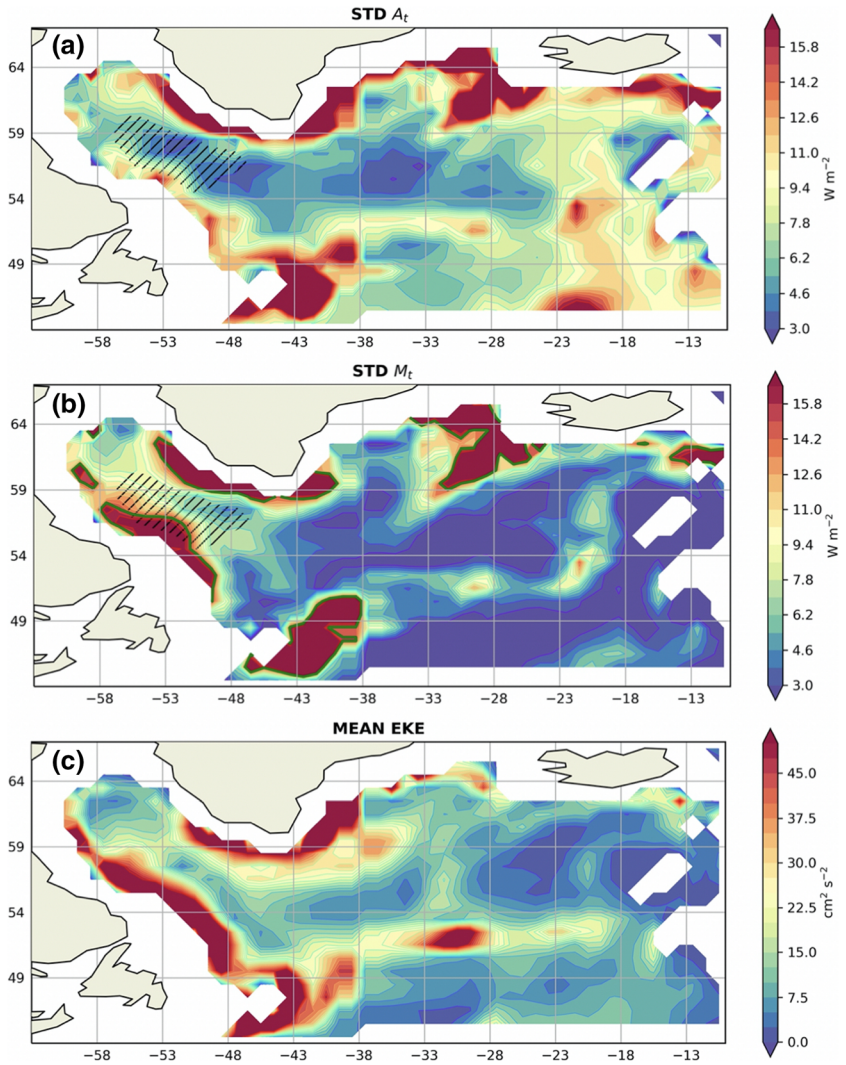

Figure 5. Standard deviation of (a) advective heat flux convergence A_t and (b) combined diffusive heat flux convergence M_t within the intermediate 700–2,000 m layer, with the hatchings showing the region of simulated deepest mixed layer depth (>2,000 m). The green contours (15 W m^{-2}) in (b) is used to delimit the highly diffusive boundary region from the interior region for further diagnosis (Figure 9d). (c) Time-mean eddy kinetic energy average within the intermediate 700–2,000 m layer.

action along the western boundary of the Labrador Sea (Figure 8a). We show here that this pattern results from a more complicated distribution of advective A_t and combined diffusive M_t fluxes (Figures 8b and 8c). While both components act altogether to warm the domain within the wide (and more quiescent) interior of the SPG, they show much greater and opposing changes in magnitude within the main dynamical areas of the domain (NAC and DWBC paths). This opposition is yet not perfect, with A_t dominating in the vicinity of Newfoundland and M_t being particularly intense along the boundary of the Labrador Sea and eastern Irminger Sea, as well as off Newfoundland. Based on the horizontal patterns of M_t standard deviation (green contours in Figures 5b and 8c), we define a "calm" interior region and an "energetic" boundary region where the vertical mixing is most intense (note that this region also matches the strongest EKE values of the intermediate; Figure 5c). This boundary region comprises three main hotspots: the northern Irminger Sea, the Labrador Sea slopes, and the Newfoundland area. We quantify the respective contributions of such interior and boundary areas to the 1996–2013 warming trend and its budget components. It is found that M_t accounts for more than 80% of the total warming trend T_t and that nearly half (42%) of this anomalous diffusive flux occurred in the *dynamical* boundary region, a substantial contribution given that this region accounts for only 8% of the SPG area (Figure 8d).

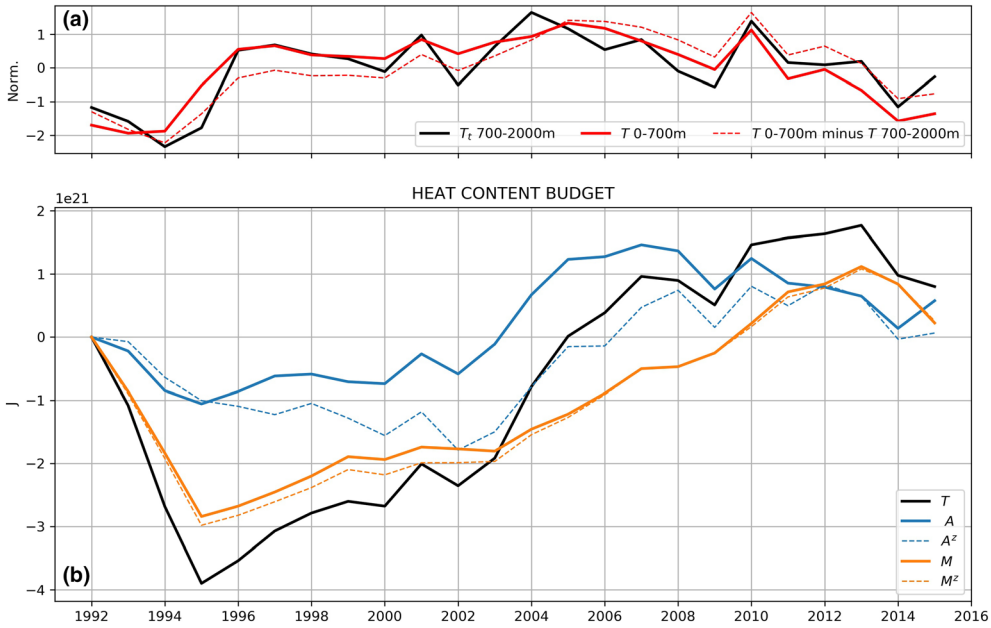

Figure 6. (a) The simulated components of the two-layer ocean model (Equation 1) in the SPG (63–10°W and 45–67°N) normalized by their respective standard deviation. (b) Cumulated heat budget components within 700–2,000 m (in J), with the tendency (T, black), advection (A, blue), and combined diffusion (M, orange). The vertical components of advection and diffusion (A^z and M^z) are shown with dashed lines.

5. Tracer Advection

A further illustration of the importance of the boundary region for the penetration of surface anomalies into the intermediate ocean is obtained with a three-dimensional advection-diffusion model whereby a passive tracer is advected by realistic spatially varying currents in the presence of a background vertical diffusion:

$$\frac{\partial \theta_d}{\partial t} - \boldsymbol{v}.\nabla\theta_d = F + \kappa\nabla^2\theta_d \tag{4}$$

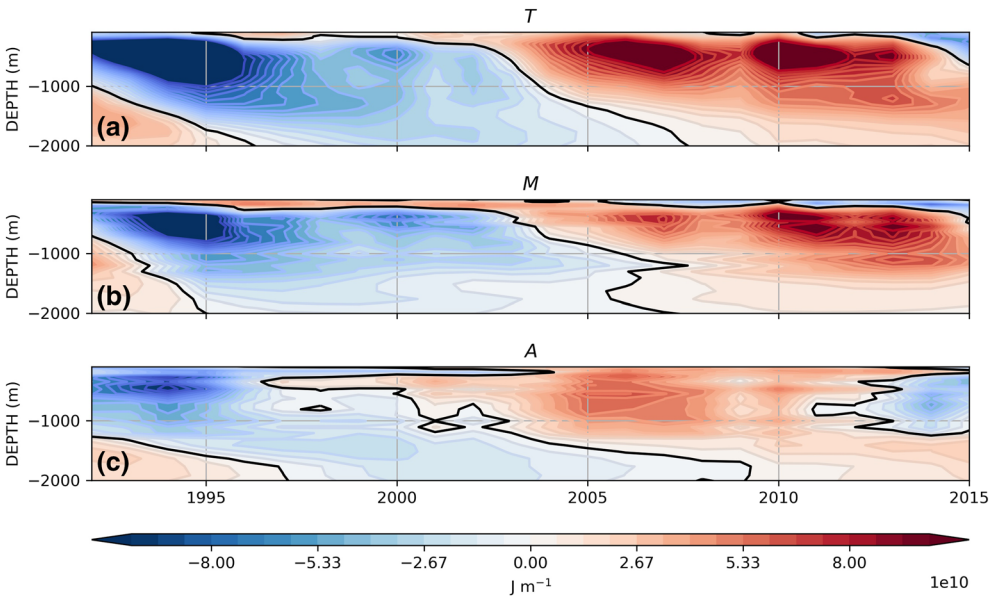

Figure 7. The depth-time diagrams of accumulated heat budget components in the SPG (63–10°W and 45–67°N) with the (a) total tendency T, (b), combined diffusion (M), and (c) and advection A.

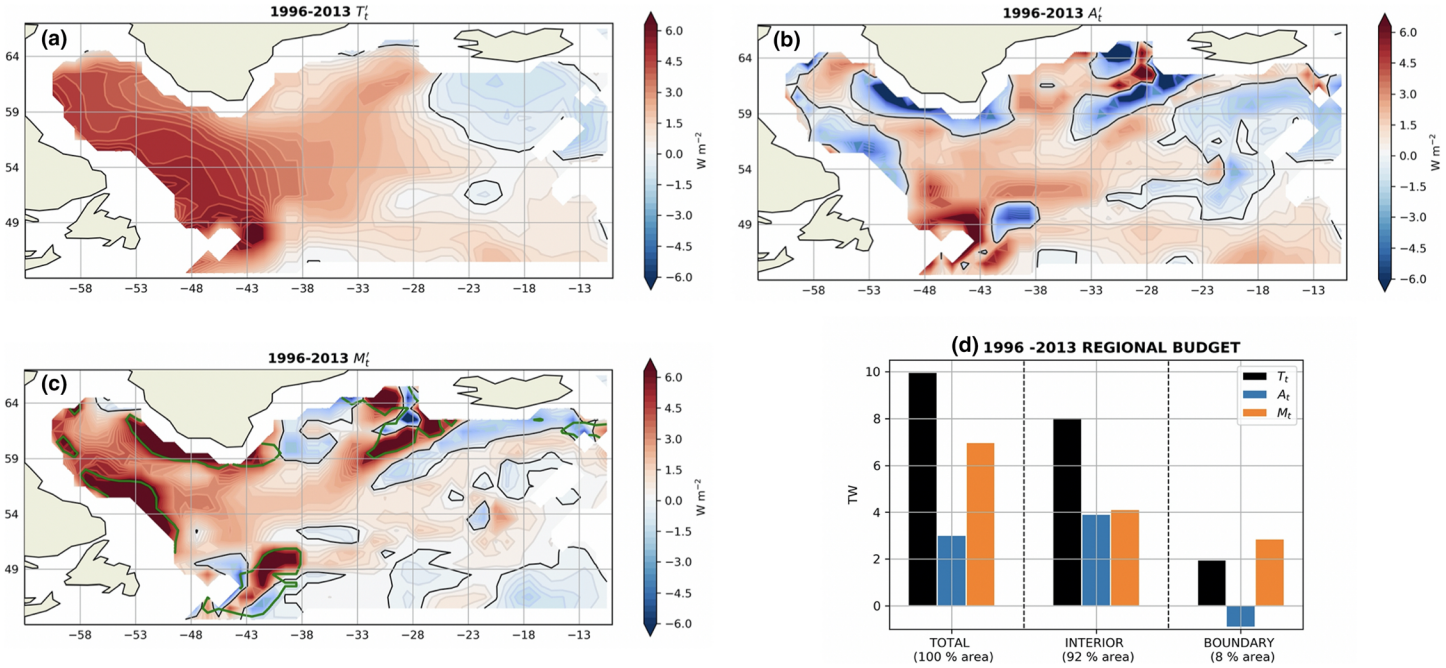

Figure 8. The spatial distribution of anomalous heat budget components within 700–2,000 m averaged during the latest warming period 1996–2013, with (a) the total tendency T_t, (b) anomalous advection A_t', and (c) anomalous combined diffusion M_t'. The green contours (5 10^{10} W) in (c) is used to delimit the highly diffusive boundary region from the interior region. The heat budget is quantified in (d) for the full SPG area and the interior/boundary areas.

which can be likewise symbolized as

$$T - A = F + M$$

and where θ_d is the temperature anomaly (tracer), v is the 3-D ocean velocity, and κ is a diffusion coefficient. The tracer is introduced in the surface layers (0–230 m) via a source, F, localized, for illustrative purposes in the East Greenland Current (green square, Figure 10a). This particular localization for F will ensure an efficient propagation of the tracer within the boundary current that encircle Greenland. The initial tracer distribution is set to zero, and Equation 4 is integrated for 10 years with a positive input of tracer, followed by a negative input for a further 10 years and finally a positive input again for 5 years. This particular succession is here chosen to mimic the surface AMV temperature signal as seen in the ECCOv4 and EN4 datasets. Realistic annual mean currents are supplied from an eddy permitting ocean general circulation model (see section 2.3). We focus here on the western portion of the SPG where the most significant downward penetration presumably occurs (see Figure 8a). This regional focus also prevents the North Atlantic Current to recirculate the tracers back to the source region and contaminate the signal in the western gyre.

In a similar way to the diagnosis of ECCOv4, we decompose the heat budget time series for the idealized model into its three components as given in Equation 4 (tendency T, advection A, and diffusion M) (Figure 9a). Given the drastic simplification inherent in the idealized model, the evolution of T reproduces the ECCOv4 pattern remarkably well, with a cooling until year 12 followed by a long-term warming until the last few years of the simulation, and an emerging cooling afterwards. Both A and M are involved with similar roles as for ECCOv4. In particular, as in ECCO, there is a phase lag between the advective and diffusive terms such that the advection peaks about 5 years before the diffusion resulting in some periods where they reinforce each other and different periods where they are in opposition. The depth-time distribution of the heat budget terms (Figures 9b–9d) is in close agreement with the observed and 1-D-modeled patterns previously described (Figure 3).

The horizontal distribution of the heat budget components averaged during the warming phase (years 11–20) of the intermediate layer is shown in Figure 10. The horizontal pattern of T_t resembles the

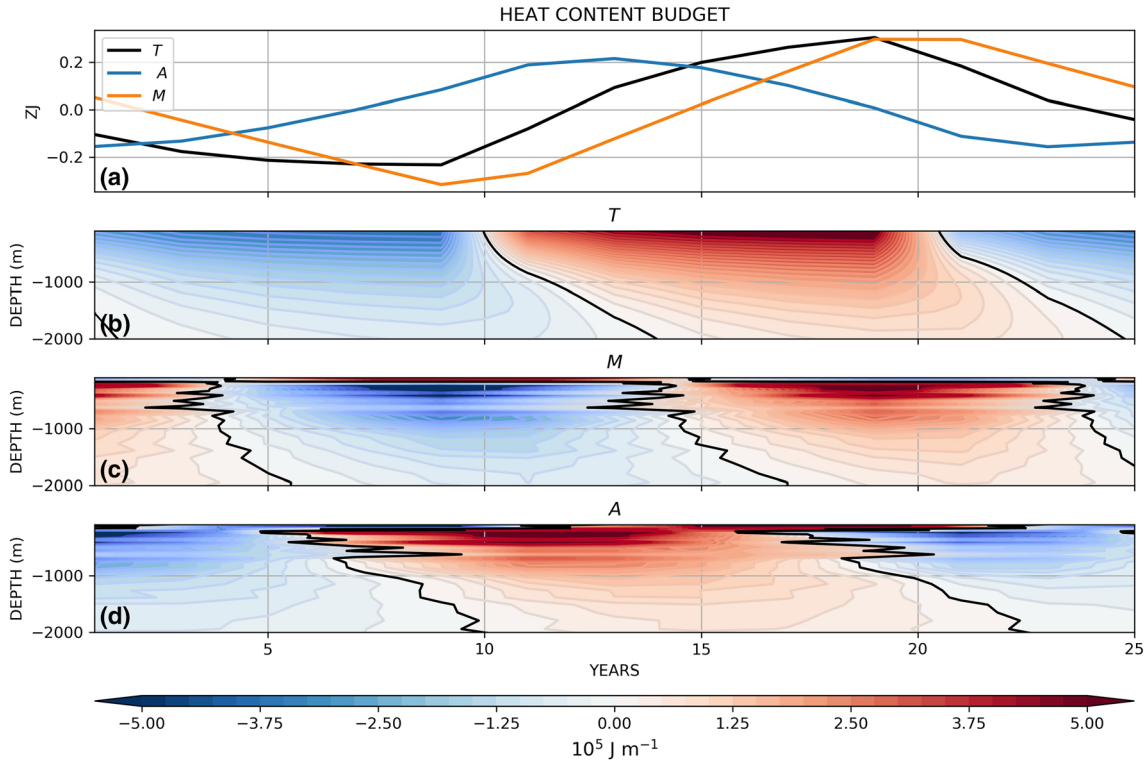

Figure 9. The heat budget in the idealized 3-D advection-diffusion model in the western SPG (70–43°W and 45–67°N) (a) cumulated heat budget components within 700–2,000 m (in ZJ), with the tendency (*T*, black), advection (*A*, blue), and diffusion (*M*, orange). The depth-time diagrams of accumulated heat budget components with the (b) total tendency *T*, (c), diffusion (*M*), and (d) and advection *A*.

observation- and state estimate-based patterns of temperature trend seen in Figures 4a and 8a, with a basin-wide warming although the heating along the western boundary of the Labrador Sea is not as strong as observed (Figure 10a). As before this pattern results from a more complicated distribution of diffusive M_t and advective A_t fluxes (Figures 10b and 10c). Both components act together to warm the domain within the wide (and more quiescent) interior of the SPG, but show much greater and opposing changes in magnitude within the main dynamical areas of the domain (NAC and DWBC paths). One difference between the idealized model and the observations/state estimate is the much stronger and more consistent anticorrelation between A_t and M_t along the boundary, which most likely relates to stronger velocities and narrower boundary currents. Based on the sign of A_t, whether it aligns with or opposes M_t (black contour in Figure 10c), we define again a "calm" interior region and an "energetic" boundary region where the vertical mixing is strongest. We still see main hotspots along the Labrador Sea slopes and the Newfoundland area, although they are more linked up into one continuous ribbon compared to the observations/state estimate. As before we quantify the respective contributions of the interior and boundary areas to the warming trend and its budget components. Once again, M_t is the main driver, accounting for more than 100% of the total warming trend T_t (with advection in fact working in the opposite sense). More than half of this anomalous diffusive flux occurs in the boundary region, a substantial contribution given that this region accounts for only 23.5% of the western SPG area of the idealized model (Figure 10d). Note that the idealized model domain is only about half the size of the domain considered for the observations and state estimates. It should also be noted that the heat budget terms and temperature anomalies seen in the idealized model are about an order of magnitude smaller than in ECCOv4. This is partly due to the smaller domain used (for area integrated quantities) and partly because of the choice of ±0.8 K for the imposed anomaly at the north eastern boundary (localized by the green square in Figure 10a).

Overall, the idealized model serves to support our hypothesis that the SPG boundary is the key area where anomalies are rapidly advected around at the surface while a slower process of diffusion transfers them to

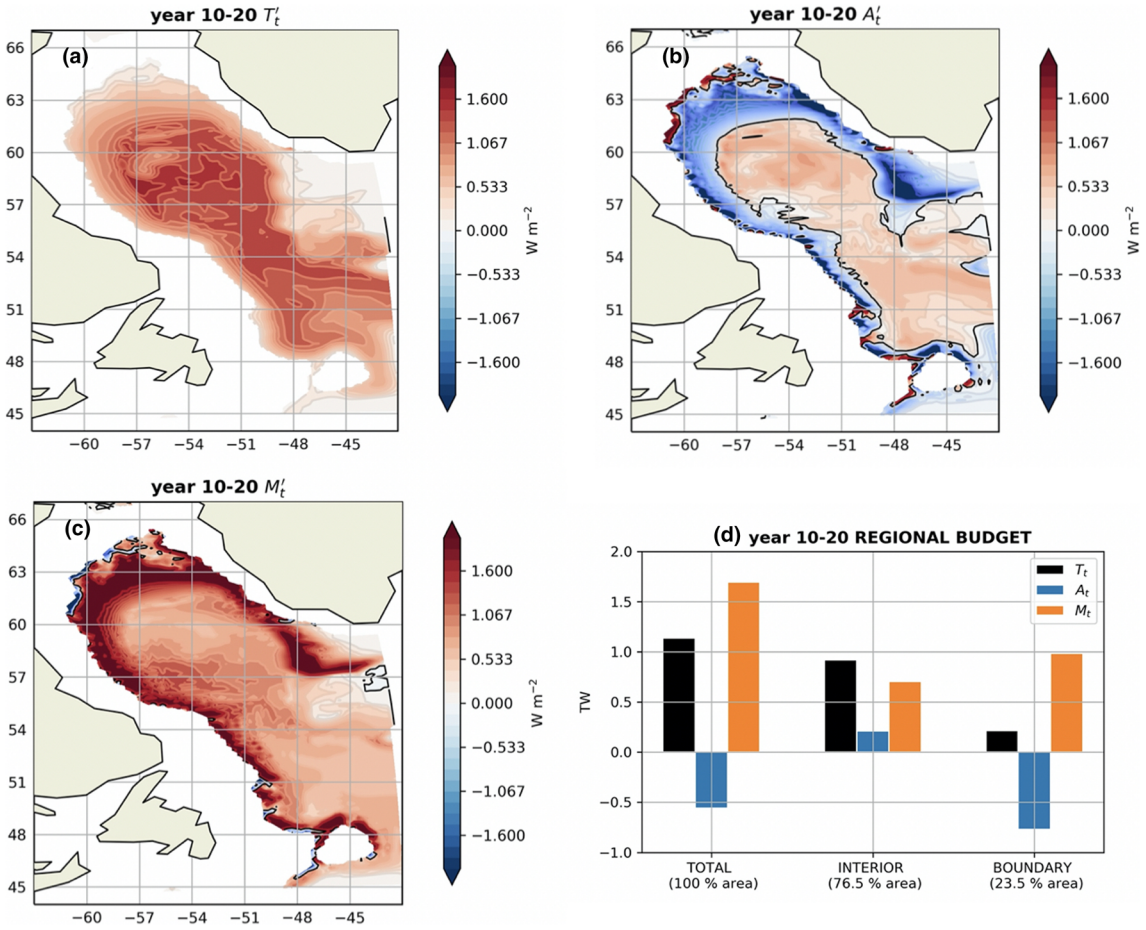

Figure 10. The spatial distribution of anomalous heat budget components within 700–2,000 m averaged during the latest warming period years 11–20, with (a) the total tendency T_t, (b) anomalous advection A_t', and (c) anomalous combined diffusion M_t'. The green square in (a) shows the location of tracer input (see section 2). The zero contour (black) in (c) is used to delimit the highly diffusive boundary region from the interior region. The heat budget is quantified in (d) for the full SPG area and the interior/boundary areas.

depth. An additional feature of the idealized model is the lack of horizontal diffusion so the interior is ventilated by a combination of horizontal advection and subsequent vertical mixing and advection. It is worth noting that if eddies were explicitly resolved in the experiment, they would contribute to mediate the tracers to depth and consequently lessen the contribution of the combined diffusion term M_t presently diagnosed in our non-eddying experiment.

6. Discussion and Conclusion

In this paper, we have provided an observation-based description of the intermediate-depth (700–2,000 m) temperature variability in the North Atlantic SPG and investigated the underlying mechanisms with realistic and idealized modeling approaches. A key driver of this variability is the downward propagation of successive and long-lasting warm and cold anomalies from the upper 0–700 m layer, which are themselves known to be driven by the decadal variability of the large-scale upper circulation and often referred to with the so-called AMV index (Desbruyères et al., 2015; Frajka-Williams et al., 2017; Häkkinen et al., 2011; McCarthy et al., 2015). While open-ocean deep convective chimneys stand as important gateways for those upper anomalies to enter the intermediate and deep ocean—and were likely a dominant one during the early-1990s event (Yashayaev et al., 2008)—the simulated vertical heat flux variability is found to be largest within energetic and bathymetry-constrained currents encircling the SPG (DWBC and NAC). In particular, vertical diffusion (which includes here the effect of convective instabilities above the upper slopes) confined along the eastern and western boundaries of the Labrador Sea, as well as advection around Newfoundland,

have likely played an important role in explaining half of the most recent warming trend observed in the region (1996–2013). Those regions are consistently those where the most substantial AMV-like and density-compensated temperature signal has been historically observed in the upper layer (Zhang & Yan, 2017). We therefore argue that the observed low-frequency temperature variability in the intermediate SPG is not solely driven by intermittent convection-restratification events in the central Labrador and Irminger seas but is also strongly influenced by boundary-intensified processes that propagate upper AMV anomalies downward.

Although such downwelling and mixing processes remains hard to decipher mechanistically with the present tools, the dominating pathways and time scales can be elucidated and reconstructed from simple modeling strategy, including a 1-D model parametrized with an effective boundary-like diffusivity and a three-dimensional advection and diffusion of tracers in a realistic time-mean boundary current field. All methodological approaches proposed herein support the hypothesis of an important role of boundary processes for the decadal-scale heat uptake of the whole intermediate layer of the SPG. Decomposing the significant contribution of boundary-focused combined diffusion to the vertical heat flux variability into underlying physical processes is beyond the scope of the first-order heat budgets proposed herein. Yet one can expect that eddy-driven mixing along heavily slanted isopycnals and direct convective instabilities above the continental slope both play important roles in injecting temperature anomalies downward. Because the multidecadal temperature signal is largely density-compensated (Mauritzen et al., 2012), results presented herein for anomalous heat content likely apply to anomalous salt content as well. The suggested continuous renewal of intermediate thermohaline properties in the SPG by surface signals implies skill for first-order predictions of the heat and freshwater reservoirs of the deep SPG from surface measurements only. While this conclusion concurs with previous model-based Lagrangian analysis of ventilation pathways in the region, it also exposes the impacts of shortcomings in the ability of the current generation of ocean and climate models to simulate multidecadal heat content variability in the North Atlantic because of excessive convection in the Labrador Sea (Marzocchi et al., 2015) and significant spurious numerical diapycnal diffusion (Megann, 2018). Finally, our study shows the importance of maintaining sustained observational networks along and across the western boundary current system of the Labrador and Newfoundland zones, including fine-scale measurements of vertical mixing near the continental slope.

Data Availability Statement

The EN4 data product used herein is freely available at https://www.metoffice.gov.uk/hadobs/en4/.

Bathymetric features were derived from the ETOPO2.v2 bathymetry product available at https://www.ngdc.noaa.gov/mgg/global/etopo2.html. The ECCOv4r3 fields used herein are freely available at: https://earthdata.nasa.gov/esds/competitive-programs/access/ecco-ocean. The annual mean velocity field from the ¼° forced ocean model are available as supporting information. These files (netcdf format) contain the zonal (u), meridional (v), and vertical (w) velocities used as input to the tracer advection program.

Acknowledgments

This study was supported by the UK's Natural Environment Research Council through the projects "Securing Multidisciplinary UndeRstanding and Prediction of Hiatus and Surge events (SMURPHS, Grant NE/N005686/1)" and "North Atlantic Climate System Integrated Study (ACSIS, Grant NE/N018044/1)" and "Transient tracer-based Investigation of circulation and Thermal Ocean Change (TICTOC, Grant NE/P019293/1). Support was also received from the OBLADY and CROSSROAD-CESAR projects funded by the French national program LEFE/INSU. Adam Blaker ran and supplied data from the ¼° forced ocean model used for the passive tracer experiments.

References

Chafik, L., Nilsen, J. E. Ø., Dangendorf, S., Reverdin, G., & Frederikse, T. (2019). North Atlantic Ocean circulation and decadal sea level change during the altimetry era. *Scientific Reports*, *9*, 1041. https://doi.org/10.1038/s41598-018-37603-6

Chen, X., & Tung, K.-K. (2014). Varying planetary heat sink led to global-warming slowdown and acceleration. *Science*, *345*(6199), 897–903. https://doi.org/10.1126/science.1254937

Cheng, L., Trenberth, K. E., Fasullo, J., Boyer, T., Abraham, J., & Zhu, J. (2017). Improved estimates of ocean heat content from 1960 to 2015. *Science Advances*, *3*, e1601545. https://doi.org/10.1126/sciadv.1601545

Colin de Verdière, A., Meunier, T., & Ollitrault, M. (2019). Meridional overturning and heat transport from Argo floats displacements and the planetary geostrophic method (PGM): Application to the subpolar North Atlantic. *Journal of Geophysical Research: Oceans*, *124*, 6270–6285. https://doi.org/10.1029/2018JC014565

Daniault, N., Mercier, H., Lherminier, P., Sarafanov, A., Falina, A., Zunino, P., et al. (2016). The northern North Atlantic Ocean mean circulation in the early 21st century. *Progress in Oceanography*, *146*(June), 142–158. https://doi.org/10.1016/j.pocean.2016.06.007

Desbruyères, D., Mercier, H., & Thierry, V. (2015). On the mechanisms behind decadal heat content changes in the eastern subpolar gyre. *Progress in Oceanography*, *132*, 262–272. https://doi.org/10.1016/j.pocean.2014.02.005

Desbruyères, D., Mcdonagh, E. L., King, B. A., & Thierry, V. (2017). Global and full-depth ocean temperature trends during the early twenty-first century from Argo and repeat hydrography. *Journal of Climate*, *30*(6), 1985–1997. https://doi.org/10.1175/JCLI-D-16-0396.1

Desbruyères, D. G., Mercier, H., Maze, G., & Daniault, N. (2019). Surface predictor of overturning circulation and heat content change in the subpolar North Atlantic. *Ocean Science Discussions*, *15*(3), 809–817. https://doi.org/10.5194/os-2019-7

Drijfhout, S. S., Blaker, A. T., Josey, S. A., Nurser, A. J. G., Sinha, B., & Balmaseda, M. A. (2014). Surface warming hiatus caused by increased heat uptake across multiple ocean basins. *Geophysical Research Letters*, *41*, 7868–7874. https://doi.org/10.1002/2014GL061456

Falina, A., Sarafanov, A., Mercier, H., Lherminier, P., Sokov, A., & Daniault, N. (2012). On the cascading of dense shelf waters in the Irminger Sea. *Journal of Physical Oceanography*, *42*(12), 2254–2267. https://doi.org/10.1175/JPO-D-12-012.1

Forget, G., Campin, J.-M., Heimbach, P., Hill, C. N., Ponte, R. M., & Wunsch, C. (2015). ECCO version 4: An integrated framework for non-linear inverse modeling and global ocean state estimation. *Geoscientific Model Development*, *8*(10), 3071–3104. https://doi.org/10.5194/gmd-8-3071-2015

Frajka-Williams, E., Beaulieu, C., & Duchez, A. (2017). Emerging negative Atlantic multidecadal oscillation index in spite of warm subtropics. *Scientific Reports*, *7*, 11224. https://doi.org/10.1038/s41598-017-11046-x

Gaspar, P., Grégoris, Y., & Lefevre, J.-M. (1990). A simple eddy kinetic energy model for simulations of the oceanic vertical mixing: Tests at station Papa and long-term upper ocean study site. *Journal of Geophysical Research*, *95*(C9), 16,179–16,193. https://doi.org/10.1029/JC095iC09p16179

Gent, P. R., & Mcwilliams, J. C. (1990). Isopycnal mixing in ocean circulation models. *Journal of Physical Oceanography*, *20*(1), 150–155. https://doi.org/10.1175/1520-0485(1990)020<0150:IMIOCM>2.0.CO;2

Good, S. A., Martin, M. J., & Rayner, N. A. (2013). EN4: Quality controlled ocean temperature and salinity profiles and monthly objective analyses with uncertainty estimates. *Journal of Geophysical Research: Oceans*, *118*, 6704–6716. https://doi.org/10.1002/2013JC009067

Gregory, J. M. (2000). Vertical heat transports in the ocean and their effect on time-dependent climate change. *Climate Dynamics*, *16*(7), 501–515. https://doi.org/10.1007/s003820000059

Häkkinen, S., Rhines, P. B., & Worthen, D. L. (2011). Warm and saline events embedded in the meridional circulation of the northern North Atlantic. *Journal of Geophysical Research*, *116*, C03006. https://doi.org/10.1029/2010JC006275

Handmann, P., Fischer, J., Visbeck, M., & Karstensen, J. (2018). The deep western boundary current in the Labrador Sea from observations and a high-resolution model. *Journal of Geophysical Research: Oceans*, *123*, 2829–2850. https://doi.org/10.1002/2017JC013702

Johnson, G. C., Lyman, J. M., & Loeb, N. G. (2016). Improving estimates of Earth's energy imbalance. *Nature Climate Change*, *6*(7), 639–640. https://doi.org/10.1038/nclimate3043

Josey, S. A., Hirschi, J. J.-M., Sinha, B., Duchez, A., Grist, J. P., & Marsh, R. (2018). The recent Atlantic cold anomaly: Causes, consequences, and related phenomena. *Annual Review of Marine Science*, *10*(1), 475–501. https://doi.org/10.1146/annurev-marine-121916-063102

Katsman, C. A., Drijfhout, S. S., Dijkstra, H. A., & Spall, M. A. (2018). Sinking of dense North Atlantic waters in a global ocean model: Location and controls. *Journal of Geophysical Research: Oceans*, *123*, 3563–3576. https://doi.org/10.1029/2017JC013329

Lauderdale, J. M., Bacon, S., Garabato, A. C. N., & Holliday, N. P. (2008). Intensified turbulent mixing in the boundary current system of southern Greenland. *Geophysical Research Letters*, *35*, L04611. https://doi.org/10.1029/2007GL032785

Le Bras, I. A.-A., Straneo, F., Holte, J., Jong, M. F., & Holliday, N. P. (2020). Rapid export of waters formed by convection near the Irminger Sea's western boundary. *Geophysical Research Letters*, *47*, 10,201–10,208. https://doi.org/10.1029/2019GL085989

Liang, X., Piecuch, C. G., Ponte, R. M., Forget, G., Wunsch, C., & Heimbach, P. (2017). Change of the global ocean vertical heat transport over 1993–2010. *Journal of Climate*, *30*(14), 5319–5327. https://doi.org/10.1175/JCLI-D-16-0569.1

Liang, X., Spall, M., & Wunsch, C. (2017). Global ocean vertical velocity from a dynamically consistent ocean state estimate. *Journal of Geophysical Research: Oceans*, *122*, 8208–8224. https://doi.org/10.1002/2017JC012985

Liang, X., Wunsch, C., Heimbach, P., & Forget, G. (2015). Vertical redistribution of oceanic heat content. *Journal of Climate*, *28*(9), 3821–3833. https://doi.org/10.1175/JCLI-D-14-00550.1

Liu, C., Allan, R. P., Berrisford, P., Mayer, M., Hyder, P., Loeb, N. G., et al. (2015). Combining satellite observations and reanalysis energy transports to estimate global net surface energy fluxes 1985–2012. *Journal of Geophysical Research: Atmospheres*, *120*, 9374–9389. https://doi.org/10.1002/2015JD023264

MacGilchrist, G. (2017). Lagrangian perspectives on ocean ventilation (PhD thesis). University of Oxford.

Madec, G., Bourdallé-Badie, R., Chanut, J., Clementi, E., Coward, A., Ethé, C., et al. (2019). NEMO ocean engine (Version 4.0). In *Notes Du Pôle De Modélisation De L'institut Pierre–simon Laplace (IPSL)*. Zenodo. https://doi.org/10.5281/zenodo.3878122

Marshall, J., Adcroft, A., Hill, C., Perelman, L., & Heisey, C. (1997). A finite-volume, incompressible Navier Stokes model for studies of the ocean on parallel computers. *Journal of Geophysical Research*, *102*(C3), 5753–5766. https://doi.org/10.1029/96JC02775

Marzocchi, A., Hirschi, J. J. M., Holliday, N. P., Cunningham, S. A., Blaker, A. T., & Coward, A. C. (2015). The North Atlantic subpolar circulation in an eddy-resolving global ocean model. *Journal of Marine Systems*, *142*, 126–143. https://doi.org/10.1016/j.jmarsys.2014.10.007

Mauritzen, C., Melsom, A., & Sutton, R. T. (2012). Importance of density-compensated temperature change for deep North Atlantic Ocean heat uptake. *Nature Geoscience*, *5*(12), 905–910. https://doi.org/10.1038/ngeo1639

McCarthy, G. D., Haigh, I. D., Hirschi, J. J.-M., Grist, J. P., & Smeed, D. A. (2015). Ocean impact on decadal Atlantic climate variability revealed by sea-level observations. *Nature*, *521*(7553), 508–510. https://doi.org/10.1038/nature14491

Megann, A., Storkey, D., Aksenov, Y., Alderson, S., Calvert, D., Graham, T., et al. (2014). GO5.0: The joint NERC–Met Office NEMO global ocean model for use in coupled and forced applications. *Geoscientific Model Development*, *7*(3), 1069–1092. https://doi.org/10.5194/gmd-7-1069-2014

Megann, A. (2018). Estimating the numerical diapycnal mixing in an eddy-permitting ocean model. *Ocean Modelling*, *121*, 19–33. https://doi.org/10.1016/j.ocemod.2017.11.001

Moat, B. I., Sinha, B., Josey, S. A., Robson, J., Ortega, P., Sévellec, F., et al. (2019). Insights into decadal North Atlantic Sea surface temperature and ocean heat content variability from an eddy-permitting coupled climate model. *Journal of Climate*, *32*(18), 6137–6161. https://doi.org/10.1175/JCLI-D-18-0709.1

Palter, J. B., Lozier, M. S., & Lavender, K. L. (2008). How does Labrador Sea water enter the deep western boundary current? *Journal of Physical Oceanography*, *38*(5), 968–983. https://doi.org/10.1175/2007JPO3807.1

Piecuch, C. G., Ponte, R. M., Little, C. M., Buckley, M. W., & Fukumori, I. (2017). Mechanisms underlying recent decadal changes in subpolar North Atlantic Ocean heat content. *Journal of Geophysical Research: Oceans*, *122*, 7181–7197. https://doi.org/10.1002/2017JC012845

Redi, M. H. (1982). Oceanic isopycnal mixing by coordinate rotation. *Journal of Physical Oceanography*, *12*(10), 1154–1158. https://doi.org/10.1175/1520-0485(1982)012<1154:OIMBCR>2.0.CO;2

Rhein, M., Rintoul, S. R., Aoki, S., Campos, E., Chambers, D., Feely, R. A., et al. (2013). Observations: Ocean. In T. F. Stocker, D. Qin, G.-K. Plattner, M. Tignor, S. K. Allen, J. Boschung, A. Nauels, Y. Xia, V. Bex & P. M. Midgley. *Climate change 2013: The physical science basis. Contribution of Working Group I to the Fifth Assessment Report of the Intergovernmental Panel on Climate Change*, *Climate Change 2013—The Physical Science Basis* (pp. 255–316). Cambridge, UK and New York, NY: Cambridge University Press. https://doi.org/10.1017/CBO9781107415324.010

Riser, S. C., Freeland, H. J., Roemmich, D., Wijffels, S., Troisi, A., Belbéoch, M., et al. (2016). Fifteen years of ocean observations with the global Argo array. *Nature Climate Change*, *6*(2), 145–153. https://doi.org/10.1038/nclimate2872

Robson, J., Sutton, R. T., Archibald, A., Cooper, F., Christensen, M., Gray, L. J., et al. (2018). Recent multivariate changes in the North Atlantic climate system, with a focus on 2005–2016. *International Journal of Climatology*, *38*(14), 5050–5076. https://doi.org/10.1002/joc.5815

Roemmich, D., Church, J., Gilson, J., Monselesan, D., Sutton, P., & Wijffels, S. (2015). Unabated planetary warming and its ocean structure since 2006. *Nature Climate Change*, *5*(3), 240–245. https://doi.org/10.1038/nclimate2513

Sayol, J., Dijkstra, H., & Katsman, C. (2019). Seasonal and regional variations of sinking in the subpolar North Atlantic from a high-resolution ocean model. *Ocean Science*, *15*(4), 1033–1053. https://doi.org/10.5194/os-15-1033-2019

Spall, M. A. (2010). Dynamics of downwelling in an eddy-resolving convective basin. *Journal of Physical Oceanography*, *40*(10), 2341–2347. https://doi.org/10.1175/2010JPO4465.1

Spall, M. A., & Pickart, R. S. (2001). Where does dense water sink? A subpolar gyre example*. *Journal of Physical Oceanography*, *31*(3), 810–826. https://doi.org/10.1175/1520-0485(2001)031<0810:WDDWSA>2.0.CO;2

Stöber, U., Walter, M., Mertens, C., & Rhein, M. (2008). Mixing estimates from hydrographic measurements in the deep western boundary current of the North Atlantic. *Deep-Sea Research Part I: Oceanographic Research Papers*, *55*(6), 721–736. https://doi.org/10.1016/j.dsr.2008.03.006

Straneo, F. (2006). On the connection between dense water formation, overturning, and poleward heat transport in a convective basin*. *Journal of Physical Oceanography*, *36*(9), 1822–1840. https://doi.org/10.1175/JPO2932.1

Talley, L. D., Feely, R. A., Sloyan, B. M., Wanninkhof, R., Baringer, M. O., Bullister, J. L., et al. (2016). Changes in ocean heat, carbon content, and ventilation: A review of the first decade of GO-SHIP global repeat hydrography. *Annual Review of Marine Science*, *8*(1), 185–215. https://doi.org/10.1146/annurev-marine-052915-100829

Vallat, R. (2018). Pingouin: Statistics in Python. *Journal of Open Source Software*, *3*, 1026. https://doi.org/10.21105/joss.01026

Van Aken, H. M., Femke de Jong, M., & Yashayaev, I. (2011). Decadal and multi-decadal variability of Labrador Sea Water in the north-western North Atlantic Ocean derived from tracer distributions: Heat budget, ventilation, and advection. *Deep-Sea Research Part I: Oceanographic Research Papers*, *58*(5), 505–523. https://doi.org/10.1016/j.dsr.2011.02.008

Walter, M., Mertens, C., & Rhein, M. (2005). Mixing estimates from a large-scale hydrographic survey in the North Atlantic. *Geophysical Research Letters*, *32*, L13605. https://doi.org/10.1029/2005GL022471

Whalen, C. B., Talley, L. D., & MacKinnon, J. A. (2012). Spatial and temporal variability of global ocean mixing inferred from Argo profiles. *Geophysical Research Letters*, *39*, L18612. https://doi.org/10.1029/2012GL053196

Yashayaev, I., Holliday, N. P., Bersch, M., & van Aken, H. M. (2008). The history of the Labrador Sea water: Production, spreading, transformation and loss. In R. R. Dickson, J. Meincke, & P. Rhines (Eds.), *Arctic-subarctic ocean fluxes: Defining the role of the northern seas in climate* (pp. 569–612). Dordrecht: Springer Netherlands. https://doi.org/10.1007/978-1-4020-6774-7_25

Yashayaev, I., & Loder, J. W. (2016). Recurrent replenishment of Labrador Sea water and associated decadal-scale variability. *Journal of Geophysical Research: Oceans*, *121*, 8095–8114. https://doi.org/10.1002/2016JC012046

Zhang, W., & Yan, X.-H. (2017). The subpolar North Atlantic Ocean heat content variability and its decomposition. *Scientific Reports*, *7*, 13748. https://doi.org/10.1038/s41598-017-14158-6